Energy & Environmental Science

PAPER

View Article Online
View Journal

Cite this: DOI: 10.1039/c9ee00085b

Materials design of perovskite solid solutions for thermochemical applications†

Josua Vieten, *[ab] Brendan Bulfin,[c] Patrick Huck,[d] Matthew Horton,[d] Dorottya Guban,[a] Liya Zhu,[e] Youjun Lu,[e] Kristin A. Persson,[d] Martin Roeb[a] and Christian Sattler[ab]

Received 9th January 2019,
Accepted 12th March 2019

DOI: 10.1039/c9ee00085b

rsc.li/ees

Perovskites are excellent candidate materials as oxygen carriers in thermochemical processes. Due to their versatile composition, it is possible to fine-tune the perovskite's properties. We present a method for the rational design of $AMO_{3-\delta}$ perovskite solid solutions with two different species on the Msite in order to tune their redox behavior. To account for the different ionic radii of different transition metal species M, two distinct ions are used in a solid solution on the A site, allowing tolerance-factor adjusted materials design. Using this methodology, we can create stable perovskites over a large range of different compositions. Leveraging the infrastructure of Materials Project, we calculate redox enthalpies for the reduction of over 240 of these $\left(A'_xA''_{1-x}\right)\left(M'_yM''_{1-y}\right)O_3$ perovskites to their brownmillerite phases based on density functional theory (DFT). We compare this data to experimentally measured data on thermodynamics of 24 of these materials to verify our theoretical framework. An empirical model is formulated for predicting the enthalpy and entropy changes as a function of the perovskites non-stoichiometry δ, which can be used to simulate the equilibrium composition as a function of temperature and oxygen partial pressure and to create a perovskite search engine based on an energetic analysis of the redox cycles. The data has been added as a contribution to MPContribs, which now includes publicly available user-controlled interactive graphs based on our theoretical and experimental data.

Broader context

Two-step thermochemical cycles are based on redox materials such as perovskites and can be used for renewable fuels production. For instance, hydrogen can be generated through water splitting, but routes to produce hydrocarbons or ammonia are envisaged as well. The heat for these processes is typically provided through concentration of solar light. It is crucial to understand the properties of these redox materials. Their thermodynamics control the reaction temperature and oxygen partial pressure. Perovskites are an attractive choice for this application since their composition is very flexible. We present how their redox properties can be fine-tuned by solid solution formation. Through rational Materials Design, we show how perovskites can be prepared for virtually any thermochemical application from low temperature air separation to water splitting. In this process, we use both theoretical and experimental data. Based on *Materials Project*, we created a user-interactive online database containing >240 perovskites. It allows retrieving materials data and enables the pre-selection of materials tailored for different applications through minimizing the total energy input using an extensive model of the redox thermodynamics. By this means, efficient redox materials can be found quicker than ever. This is an important step towards more efficient renewable fuels production.

[a] *Institute of Solar Research, Deutsches Zentrum für Luft- und Raumfahrt/German Aerospace Center, Linder Höhe, 51147 Köln, Germany. E-mail: Josua.Vieten@dlr.de*
[b] *Faculty of Mechanical Science and Engineering, Institute of Power Engineering, Professorship of Solar Fuel production, TU Dresden, 01062 Dresden, Germany*
[c] *Professorship for Renewable Energy Carriers, ETH Zurich, 8092 Zurich, Switzerland*
[d] *Energy Technologies Area, Lawrence Berkeley National Laboratory, Berkeley, USA*
[e] *State Key Laboratory of Multiphase Flow in Power Engineering (SKLMF), Xi'an Jiaotong University, Xi'an, Shaanxi 710049, China*

† Electronic supplementary information (ESI) available: Experimental and theoretical thermodynamic, fit parameters, and derivation of thermodynamic equations used. See DOI: 10.1039/c9ee00085b

Introduction

Materials discovery has traditionally relied on intuition-based trial and error. In the past few decades, however, computational methods such as density functional theory (DFT) have gained ground allowing for the prediction of materials properties, prior to synthesis and characterization. Hence, screening of large sets of materials for target properties has been made possible in a short amount of time. Materials databases such as *Materials Project* produce such data and make it available to

the public, along with associated analysis algorithms and codes.[1–3] Numerous applications reliant on functional materials have benefitted from such resources,[4,5] from thermoelectrics, photovoltaics, and electrodes to photocatalysts. Two-step thermochemical processes are known as a means to store and convert energy from renewable sources such as solar energy. One of the most well-known of these processes is based on ceria ($CeO_{2-\delta}$) as a redox material, which – as a first step – is heated to 1400–1500 °C under low oxygen partial pressure, and undergoes partial reduction under formation of oxygen vacancies. This cerium oxide with non-stoichiometry δ is then re-oxidized exothermically in a second step at lower temperature, for instance with steam as an oxidant to generate hydrogen.[6] The heat to drive the endothermic process at high temperature can be supplied as concentrated solar power (CSP), allowing the conversion of solar energy into a fuel ("solar fuel") with high energy density. Besides water, other possible oxidants for the low temperature step include carbon dioxide which is reduced to carbon monoxide,[7] and air which is separated into oxygen and a mostly inert stream of nitrogen, argon, and trace gases.[8] To form liquid solar fuels, the as-produced hydrogen can be combined with carbon monoxide as syngas to prepare hydrocarbons such as kerosene in the Fischer–Tropsch process or through methanol-based routes,[7,9–11] or hydrogen can be used in combination with nitrogen to form ammonia in the Haber–Bosch process.[12]

However, ceria is not an ideal candidate material, due to different thermodynamic properties of each reaction.[13] For instance, air separation requires a much lower oxygen affinity of the partially reduced oxide than water splitting. Moreover, practical constraints of reactor engineering set different boundary conditions at each CSP plant, such as different reduction temperatures and pressures. Consequently, engineering of ceria by introducing dopants has been attempted,[14–16] and alternative materials such as ferrites and perovskites have been proposed.[17–21]

Perovskites are compounds of at least two different metals and oxygen. They are especially appealing as redox materials, as these compounds with the general composition $AMO_{3-\delta}$ show temperature and oxygen partial pressure dependent non-stoichiometric oxygen uptake and release, allowing for fast redox kinetics due to high lattice oxygen ion diffusion rates.[13,22,23] Moreover, stable perovskites exist for many different combinations of A and M metals, where A is typically an alkaline, alkali, or rare earth metal, and M is usually a transition metal (however some main group elements such as Al, Ga, or Bi can be incorporated as well[19,24]). By changing the composition, the perovskite's thermodynamic redox properties, especially the change in redox enthalpy ΔH and the entropy ΔS, are modified. Also, it is possible to create solid solutions with mixed species on the A and M lattice sites denoted by $\left(A'_xA''_{1-x}\right)\left(M'_yM''_{1-y}\right)O_{3-\delta}$, in order to fine-tune the redox properties and crystal structure of these perovskites.[25] This leads to a very large number of possible perovskite compositions, where identifying the optimal formulation becomes challenging. In the following, we present a rational way to design perovskites as redox materials based on simple geometric considerations such as the Goldschmidt tolerance factor, and the reduction potentials of different transition metal ions.[26] We show how by using a well-defined mixed occupation of the A and M lattice sites, the thermodynamic properties and the perovskite phase stability can be controlled accurately and systematically. By comparing the resulting theoretical materials screening to experimental data, we verify our model. The expected non-stoichiometry or oxygen release and uptake as a function of temperature and oxygen partial pressure can be derived from our thermodynamic data for a large set of materials (>240 DFT and 24 experimental datasets). The results of the screening including thermodynamic data are publicly available as interactive plots in the tool *RedoxThermoCSP* through *Materials Project* as a contribution to *MPContribs*.‡.

Perovskite design principles

Perovskite phases consist of a cation A, and a relatively smaller cation M, as well as oxygen anions to achieve charge neutrality, which may require a non-stoichiometry expressed by δ. As the *A* cation is larger in ionic radius than the M cation, it typically carries a smaller positive charge. Therefore, most A cations feature group I or II elements or rare earth metals, whereas M cations are often transition metal species. Many transition metals show interesting redox chemistry, whereas the charge of alkali and alkaline metals is always +I or +II, respectively, with the exception of rubidium and cesium suboxides.[27] We therefore assume the charge of the A cations to be maintained independent of temperature and oxygen partial pressure, whereas the M site is considered redox-active. The A and M lattice sites in $AMO_{3-\delta}$ may also be occupied partially by more than one type of A and M species, which in the case of two different species on each site we denote by A′/A″ and M′/M″, respectively. These mixed perovskites exhibit randomly distributed A and M species (ideal solid solutions), as well as ordered superstructures in some cases.[28–30] In our models, we assume statistical (= random) distribution of these species in order to use a standardized model for all cases. This is a valid assumption according to Goldschmidt's rules on the formation of solid solutions, which postulate that the difference in ionic radii should not exceed approx. 15% to favor isomorphic mixtures.[26] This is the case for the vast majority of species in our study. Moreover, in order to keep the DFT computational expense manageable, we perform calculations with a maximum of two different species on each perovskite site. As discussed later, however, we approximate the solid solutions with ordered supercells in our DFT calculations, which may introduce some errors if these deviate in energy from the actual disordered structures.

The composition of a perovskite solid solution with different sets of A and M cations and an oxygen anion non-stoichiometry δ can be described by denoting the charge of the transition metal species by n, resulting in the general composition

$$\left(A'_xA''_{1-x}\right)^{(6-n)+}\left(M'_yM''_{1-y}\right)^{(n-2\delta)+}O_{3-\delta} \quad (1)$$

‡ https://materialsproject.org/mpcontribs and https://materialsproject.org/mpcontribs/redox_thermo_csp

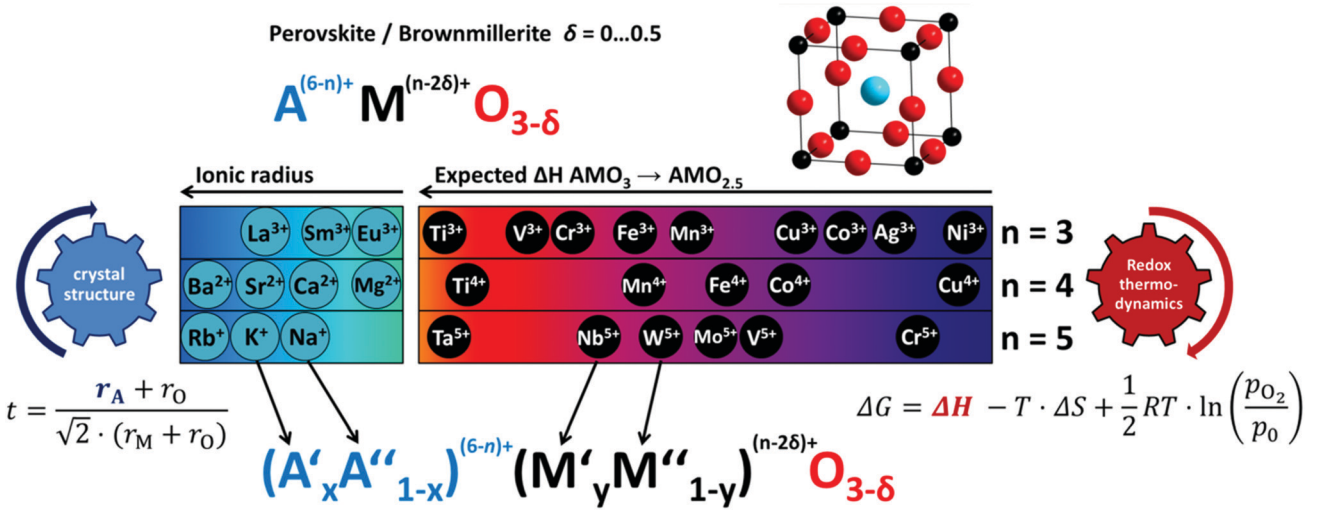

Fig. 1 Creating perovskite solid solutions with two different M species M′ and M″ and two different A species A′ and A″. The redox enthalpy is mainly governed by the transition metal species M, and can be fine-tuned by mixing different transition metals. To obtain a stable crystal structure, A site species are chosen to match a target tolerance factor t.

with n = 3, 4, or 5 in our case, and δ = 0...0.5 (with possible exceptions from this non-stoichiometry range, which are not covered in our study). To find A′/A″ and M′/M″ species and their stoichiometric ratios x and y in order to form a stable perovskite with well-defined redox properties, we use the following materials design approach (see Fig. 1):

1. Tolerance factor engineering
– Define a stable perovskite structure
2. Selection of M site species
– Define reducibility (redox thermodynamics)
3. Selection of A site species
– Match ionic radii to reach target tolerance factor

We iterate over a number of different n and t (tolerance factor) values in order to define a set of stable perovskite compositions with different redox properties. Selected perovskites with n = 4 are also subjected to an experimental materials screening, whereas a larger set of perovskites with n = 3, 4, and 5 are studied using theoretical methods alone.

Tolerance factor engineering

The tolerance factor, introduced by V. M. Goldschmidt as early as 1926, is a purely geometrical figure using the ionic radii r_A, r_M, and r_O of the ions in the perovskite lattice to predict its stability.[26] Under the assumption of ideal solid solution formation with statistically distributed species, we can calculate an adapted tolerance factor for perovskites given in eqn (1) using the weighted average of the ionic radii:

$$t = \frac{[r_{A'} \cdot x + r_{A''} \cdot (1 - x)] + r_O}{\sqrt{2} \cdot ([r_{M'} \cdot y + r_{M''} \cdot (1 - y)] + r_O)} \quad (2)$$

The ionic radii are taken from Shannon[31] and unknown values for unusual species such as Cu^{4+} or highly coordinated Mg^{2+} are estimated using the Pauling bond strengths (see ESI†).[32] Moreover, we exclude temperature effects in our first approximation of expected crystal structures. The tolerance factor typically increases with increasing temperature, but the effect is negligible for structures in equilibrium at room temperature.[33] For partially reduced phases, oxygen vacancies are assumed to exhibit a radius r_{vac} = 131 pm according to Chatzichristodoulou *et al.*[34] The tolerance factor of an undistorted cubic perovskite lattice is t = 1.00, and deviations from this value will result in distorted perovskite lattice types. For instance, by gradually replacing Fe^{4+} by Mn^{4+} cations in $SrFeO_{3-\delta}$, the crystal structure gradually changes from orthorhombic and tetragonal variants to cubic perovskites, and from those to rhombohedral and finally hexagonal structures.[25] In some cases, rhombohedral structures form as mixtures between cubic and hexagonal stacking.[25] The formation of tetragonal and different forms of orthorhombic crystal structures occurs at $t < 1.00$ and is associated with a tilt of the octahedral coordination spheres, in which a large number of different tilt systems is possible.[35–37] If the distortion becomes too large, other structure types than the perovskite structure and its variants may become more stable. In addition to the ionic radii of different cation species, the reduction of transition metal ions leads to an increase in their ionic radii, which decreases the tolerance factor according to eqn (2).[25] In order to avoid phase transitions or decomposition during reduction, the tolerance factor in the fully oxidized state should not be too low in order to leave room for the stronger distortion of the reduced phase. For example, $Ca_{0.8}Sr_{0.2}MnO_{3-\delta}$ with its larger average A site ionic radius shows an improved redox performance and a greater stability range than $CaMnO_{3-\delta}$, which becomes unstable if the Mn^{4+} ions are reduced and increase in their radii.[38] To exclude the effect of different crystal structures and distortions on the redox performance of the materials in the screening performed here, we define fixed tolerance factors w.r.t. the oxidized perovskite state. These tolerance factors can be maintained for different solid solutions with different M site composition by adjusting the A site composition (see Fig. 2) through solving eqn (2) for x. The result is a set of perovskites with different redox thermodynamics and lattice

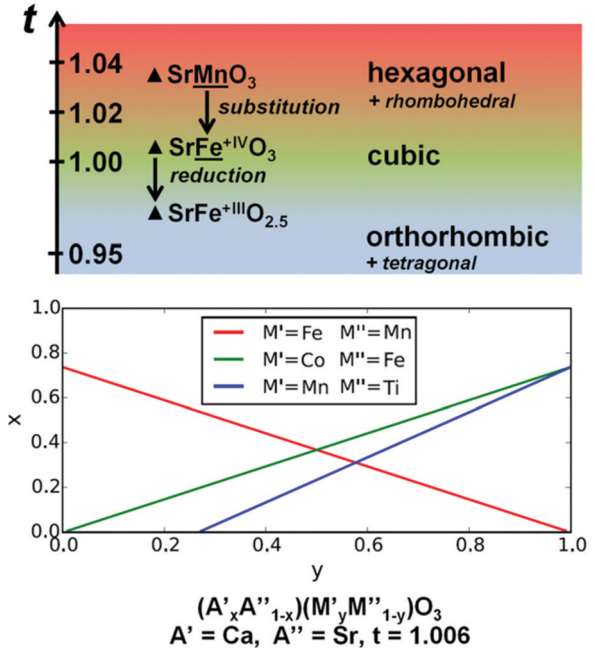

Fig. 2 Tolerance factors of different pure perovskites (top) and the expected crystal structures. Substitution or partial reduction of the involved species may induce a phase change. For the case of solid solutions (bottom), a constant tolerance factor (here 1.006) in the oxidized state can be maintained if the ratio of A′ and A″ and M′ and M″ ions is changed simultaneously.

parameters, but the same crystal system and type of phases. In this way, we favor stable perovskites with a large range of different M site compositions. Although small phase changes leading to different oxygen vacancy ordered orthorhombic and tetragonal structures occur during reduction, the atoms do not undergo major re-arrangement, and the redox reactions should occur at high rates.[22,25,39]

The Goldschmidt tolerance factor, however, is only suitable as a first approximation of the perovskite structure and stability, as real structure formation is not only governed by geometric considerations, but also by bond strengths, electronegativity differences, and the effect of different spin states.[25,40] However, despite the simplifications made in order to reduce the parameter space of the materials screening process, it allows us to examine many stable perovskite oxides.

Selection of M site species

Transition metal species can be ranked according to their expected reducibility (= their readiness to lose oxygen), for instance by comparing the redox enthalpies for the reduction of perovskites with the same A species but different M species from the perovskite to the respective brownmillerite phases. We use data from Materials Project to do so, and if no data is available for the perovskite/brownmillerite pair, we compare the redox enthalpies of oxides with only one metal species with the same oxidation states as the perovskites and brownmillerites in our study.[3,41] This initial step enables the ordering of the transition metal species according to their reducibility for the definition of M′ and M″ species in the solid solutions (see Fig. 1). Through selecting different M site species, we obtain a set of perovskites with different reduction potentials which may be further tailored for different applications. For example, in many cases, the ideal redox enthalpy for a specific application would be situated somewhere in-between. For this purpose, we tune the reduction potential of the oxidized phase (or the oxygen affinity of the reduced phase) by creating solid solutions with mixtures of two different transition metal species (see Fig. 2). In the calculation of the tolerance factor, the ionic radii are obtained for coordination number CN = 6 for both transition metal ions M′ and M″. In an earlier publication by the authors, it was demonstrated that the redox enthalpy of $SrFeO_3$–$SrMnO_3$ solid solutions can be tuned by adjusting the Fe/Mn content.[25] Within this work, we extend this method of design to a larger set of solid solution phases. While the choice of M site species provides the main descriptor for the perovskite's reduction enthalpies, different A site species offer only small perturbation on the redox thermodynamics but can greatly impact the crystal structure and perovskite stabilities. In the following, we explain how the crystal structure can be modified through targeted selection of A site species.

Selection of A site species

For the A site species, we choose a variety of species with the appropriate charges, and order them by ionic radius. We pick those species which most likely form stable perovskites in combination with transition metals (see also: tolerance factor engineering). The CN of A′ and A″ species is 12 in an ideal perovskite structure, but formally decreases in the case of distorted phases. We empirically found for $SrFeO_{3-\delta}$–$SrMnO_{3-\delta}$ solid solutions that the observed perovskite crystal structures are best explained under the assumption of a mixed CN 12 and CN 10 with a ratio of CN 12/CN 10 = 0.8. This is somewhat arbitrary, but it leads to reasonable empirical results. For example, a CN of 12 yields a tolerance factor of $SrFeO_{2.81}$ (its composition after synthesis in air[42]) of 1.001, which corresponds to a near-ideal cubic perovskite structure. However, the material forms as a mixture of orthorhombic and tetragonal phases.[39] By assuming a slightly lower coordination of the A site ions, which decreases the average A ionic radii by 1 to 2%, we empirically reach more realistic stability limits of different phases in the $SrFeO_{3-\delta}$–$SrMnO_{3-\delta}$ system in good agreement with experimental results.[25] However, the tolerance factor may not the only factor determining the crystal structure, for example, it may be argued that the crystal ionic radii measurement exhibit error bars sufficient to explain the discrepancy. Other work may cite slightly different tolerance factors for the species discussed here, however the relative differences in tolerance factors between different phases should nevertheless be comparable. We select Na^+, K^+, and Rb^+ as alkali metal species in the system n = 5, and Ca^{2+}, Sr^{2+}, and Ba^{2+} for n = 4, as these lead to the formation of stable perovskites with many transition metal species. Additionally, we tentatively use Mg^{2+} as a potential constituent of perovskites, but phases with high magnesium content on the A site may only be stable under high pressure.[43] As rare earth species, we select those lanthanides which show

no stable +4 oxidation state in order to achieve a well-defined oxidation state of +3. Moreover, we exclude Pm as it has no stable isotopes, and Gd and all heavier elements, as they show very small ionic radii (''Gadolinium break''[44]) which penalizes the likelihood to obtain stable perovskites in combination with most transition metals. It is also possible to use perovskites with a mixed redox state on the A site, for instance lanthanum and strontium (LSMA perovskites[45]), but this is beyond the scope of this study and already well explored, mainly due to the application of such perovskites in solid oxide fuel cells.[45–47]

Experimental and theoretical methods

Over 240 perovskite compositions in addition to the respective brownmillerite phases are selected for computation. The DFT calculations are executed using crystal structures with defined compositions but generic lattice constants as inputs. We use cubic unit cells in space group 221 ($Pm\bar{3}m$) as prototypes for the AMO_3 perovskite cells and orthorhombic cells in space group 46 (*Ima*2) for the $A_2M_2O_5$ brownmillerites. In order to calculate solid solutions in DFT, it is necessary to remove partial occupancies by expanding the structures as corresponding supercells. For solid solutions such as $Ca_{0.29}Sr_{0.71}FeO_{3-\delta}$, an extremely large supercell would be required for an accurate representation of the stoichiometry without using partial occupancies, hence all occupancies are discretized by rounding them to fractions of 1/8. The error in stoichiometry introduced by this simplification is $<1/16$, and fortuitously, all structures can be represented using $2 \times 2 \times 2$ supercells of the original structural prototypes, yielding a maximum of 144 atoms for the brownmillerite supercells which is still manageable. The supercells are created using the python™ library *pymatgen* (Python Materials Genomics, www.pymatgen.org).[48] To find potentially stable perovskite compositions within this framework as described before, target tolerance factors t = 0.945, 1.0, and 1.015 are set for the fully oxidized perovskite solid solutions with n = 3, 4, and 5, respectively. The target tolerance factors are chosen such that as many stable isomorphic solid solutions are found as possible within this group of perovskites with different n. Additionally, compositions with t = 0.995, 1.006, and 1.015 are calculated for n = 4 in order to match the materials screened experimentally and study the effect of different tolerance factors on the redox enthalpies. The M metal species are combined using incremental stoichiometries as multiples of 1/8, and the A site composition is calculated accordingly to match the target tolerance factor. As illustrated in Fig. 1, two species with similar reducibilities are combined in different ratios, the corresponding A metal species are found by solving eqn (2) for x, and the resulting compositions are discretized by rounding them to multiples of 1/8. In addition to these solid solutions, pure AMO_3 perovskites and the respective brownmillerites are calculated with their compositions being permutations of all A species with all M species within each perovskite system n. All DFT calculations are computed using *MPComplete* within *Materials Project*, which uses *atomate* and *FireWorks* to submit workflows which are handled using the Vienna ab initio simulation package (VASP).[49–52] Calculations are performed using the projector-augmented wave method in the generalized gradient approximation (GGA) functional within the Perdew–Burke–Ernzerhof (PBE) framework.[53–55] By combining GGA and GGA + U calculations as explained in detail by Jain *et al.*,[41] the formation enthalpies of the perovskites and brownmillerites are calculated, allowing to retrieve the redox enthalpy for the full reduction from the perovskite to the brownmillerite phase, which is then normalized per mol of monatomic oxygen O. All calculated materials are added to the database in *Materials Project* and the materials are listed in the ESI† including hyperlinks to the corresponding Materials Project entries, which can also be retrieved using the DOI: 10.17188/1475589 to access further data.[56] It is noted that materials which were already present in the Materials Project database prior to this work are only replaced if our newly calculated materials are more stable according to their energy above the convex hull (E_{hull}). For this reason, some redox pairs used within this work contain materials with unit cells differing from the superstructures explained before, if those other structures are calculated to be more stable.

The experimental data is retrieved by synthesizing solid solutions and analyzing their thermodynamics using the van't Hoff method in thermogravimetric experiments. 5.0 mmol of each of the 24 perovskite phases are synthesized using a citric acid auto-combustion method explained in detail in the literature and in the ESI.† [57] This synthesis method is sol–gel based and yields a fine oxide precursor powder, which is then treated at high temperature in alumina crucibles using three steps at 800–1300 °C (or 800–1100 °C in the case of Co containing solid solutions due to their low melting point and interaction with the alumina crucibles). The resulting materials are powdered using a pestle and the phase formation is verified using X-ray diffraction as specified in the ESI.† With the help of different oxygen partial pressures set by changing the input gas mixture ratio and by changing the temperature in a silicon carbide furnace, the mass change of the samples under different redox conditions is observed using a NETZSCH thermobalance model STA 449 F3 Jupiter. As the mass change corresponds to the release or uptake of oxygen in these samples, equilibrium data showing the change in non-stoichiometry $\Delta\delta$ is gathered and converted to values for ΔH and ΔS using the van't Hoff method as described in the ESI.† We assume that the change in enthalpy and entropy depends only on the non-stoichiometry $\Delta\delta$, irrespective of how this non-stoichiometry was reached (temperature or pressure variation). This step may induce some error, as the enthalpy is temperature dependent, but for a large scale screening it was necessary to limit the amount of measurement time per material in the TGA. Measuring $\Delta H(\delta,T)$ instead of just $\Delta H(\delta)$ would increase the measurement time per material from days to weeks. Moreover, we do not consider enthalpy–entropy compensation.[58]

All theoretical and experimental datasets of redox thermodynamics are contributed to the *RedoxThermoCSP* database as a part of the user contribution interface *MPContribs* of Materials Project (https://materialsproject.org/mpcontribs).[2] The data is presented in user-controlled interactive graphs called *Isographs* based on theoretical and experimental functions for $\Delta H(\delta)$,

$\Delta S(\delta)$ and $\delta(T,p_{O_2})$. Based on the Gibbs–Helmholtz equation, ΔG can be calculated. *Vice versa*, by assuming $\Delta G = 0$ (*i.e.* equilibrium conditions), we can find the equilibrium temperature and oxygen partial pressure leading to a certain redox extent. Hence, isobars and isotherms describing δ are obtained as a function of T or p_{O_2}, respectively, based on the theoretical and experimental data. Moreover, we can find p_{O_2} as a function of T for fixed values of δ ("isoredox" graph). Additionally, we show graphs of $\Delta H(\delta)$ and $\Delta S(\delta)$ and Ellingham diagrams showing ΔG^0 at the reference oxygen partial pressure $p^0 = 1$ bar as a function of the temperature. All graphs can be zoomed in and out, and the ranges as well as parameters such as temperature, oxygen partial pressure and the non-stoichiometry δ can be changed freely by the user within a certain pre-defined window. The source code of RedoxThermoCSP is available on GitHub.§ User interaction was implemented using an HTML front end and JavaScript, and the interaction within the python code was performed using Django. Calculation of the equilibrium state for each of the >240 materials is a time-consuming process, prohibiting on-the-fly selection of operating conditions. Therefore, we pre-defined reasonable values for T_{red}, p_{red}, T_{ox}, and p_{ox}, resulting in a list of over 10 500 pre-defined parameters with calculated equilibrium states. To calculate the energy demand of a redox cycle, we assumed a linear change of T and $\ln(p_{O_2})$ and defined N equidistant sets of T and p_{O_2} between T_{ox}/p_{ox} and T_{red}/p_{red} at which the equilibrium state was calculated to yield ΔH_n and δ_n. The integral of the redox enthalpy was then calculated stepwise as a discretized integral with $N = 20$ to obtain an accurate approximation. The heat capacity was also calculated as a step integral. We did not calculate the integral directly because of the computationally challenging task of determining the point at which the Gibbs–Helmholtz equation is zero owing to the complexity of the involved functions for ΔH, ΔS, and δ in theoretically calculating these properties. For the analytical fit functions derived for the experimental datasets, we instead directly calculated the integral. Throughout this work, we only used results for which the integral over the redox enthalpy was larger than zero, as a negative energy input indicates that the material is not reduced but oxidized under the given conditions or that it is highly unstable in the oxidized state. Moreover, as mentioned in the documentation for the *RedoxThermoCSP* app, we excluded materials for the energetic analysis that were likely to be very unstable or difficult to form for chemical reasons. These materials included materials with a tolerance factor below 0.90, those with covalent V–O bonds, and alkali molybdenates with expected low melting points.[59]

Results and discussion

DFT-based materials screening

Out of over 250 submitted perovskite structures and the same amount of brownmillerites, over 240 redox pairs from perovskite to brownmillerite were successfully calculated, with only a very small amount of the input structures resulting in divergent calculations and errors. The crystal structures and lattice parameters of the computed solid solution phases show cell volumes generally in good agreement with Vegard's law (see the example in the ESI†),[60] with small deviations due to the discretization. The resulting redox enthalpies for the reduction from perovskite to brownmillerite span a wide range from −340 to 706 kJ per mol of oxygen (kJ mol_O^{-1}), with over 50% in the range from 50 to 400 kJ mol_O^{-1}, which is the most relevant range for thermochemical applications. If the species in this enthalpy window are ranked from low to high redox enthalpy, the maximum difference between two consecutive entries is 17 kJ mol_O^{-1} with an average of 2.5 kJ mol_O^{-1}, which showcases the possibility of fine-tuning the redox enthalpy of perovskites using tolerance-factor adjusted solid solutions. 7% of the materials show redox enthalpies below 0 kJ mol^{-1} for the reduction reaction, signifying that the oxidized phase is highly unstable and can only be obtained under extreme conditions. These include materials such as $SrCuO_{3-\delta}$, for which it has been shown experimentally that it can only be oxidized to some extent leaving a significant remaining δ,[61,62] or some magnesium-containing phases which would be more stable in non-perovskite structures according to their tolerance factors. For the most part, however, we find a large range of perovskites with tolerance factors indicating a stable perovskite structure under redox conditions (see Fig. 3). All crystal structures and further data including details on the calculation with initial and final structures are available through *Materials Project*. A list of all material pairs including their redox enthalpies, tolerance factors, and their identifiers (MP IDs) with links to the materials details page on the *Materials Project* is given in the ESI.†

The effect of the tolerance factor of the oxidized phases on the redox enthalpies is studied exemplarily for solid solutions with $n = 4$. In general, a lower tolerance factor seems to correlate with a lower redox enthalpy in many cases. As long as the tolerance factor is within the stability range of cubic perovskites and orthorhombic distorted variants and the overall charge of the A site cations is maintained, the M site composition in most cases has a stronger effect on the redox properties than the tolerance factor. However, by maintaining a constant tolerance factor, we minimize the effect of different tolerance factors and crystal structures, and thus ensure that the perovskite phases and its oxygen deficient variants do not decompose during oxidation or reduction within the window of $\delta = 0...0.5$. To study the redox behavior of perovskite solid solutions more in detail, we examine, as an example, the solid solution phase space (Ca–Sr–Ba)(Ti–Mn)$O_{3-\delta}$ (see Fig. 4). While $AMnO_3$ is significantly easier to reduce than $ATiO_3$, the redox enthalpies of solid solutions between those two phases are not proportional to the Ti content. If a small amount of the Mn^{4+} ions is replaced by Ti^{4+}, the redox enthalpy does not increase notably. It only increases significantly if the Ti content is larger than 40–60%.

Instead of a linear increase of ΔH as a function of the Ti concentration, one can observe two distinct regimes, one with ≥50% Ti concentration, and one with ≤50% Ti content. ΔH in each of these regimes appears to depend linearly on the Ti concentration, as indicated by the green dashed lines in Fig. 4. The trend lines intersect at 50% Ti concentration. Similar trends, where two distinct regimes are identified as a function

§ https://github.com/materialsproject/MPContribs/tree/master/mpcontribs-users/mpcontribs/users/redox_thermo_csp

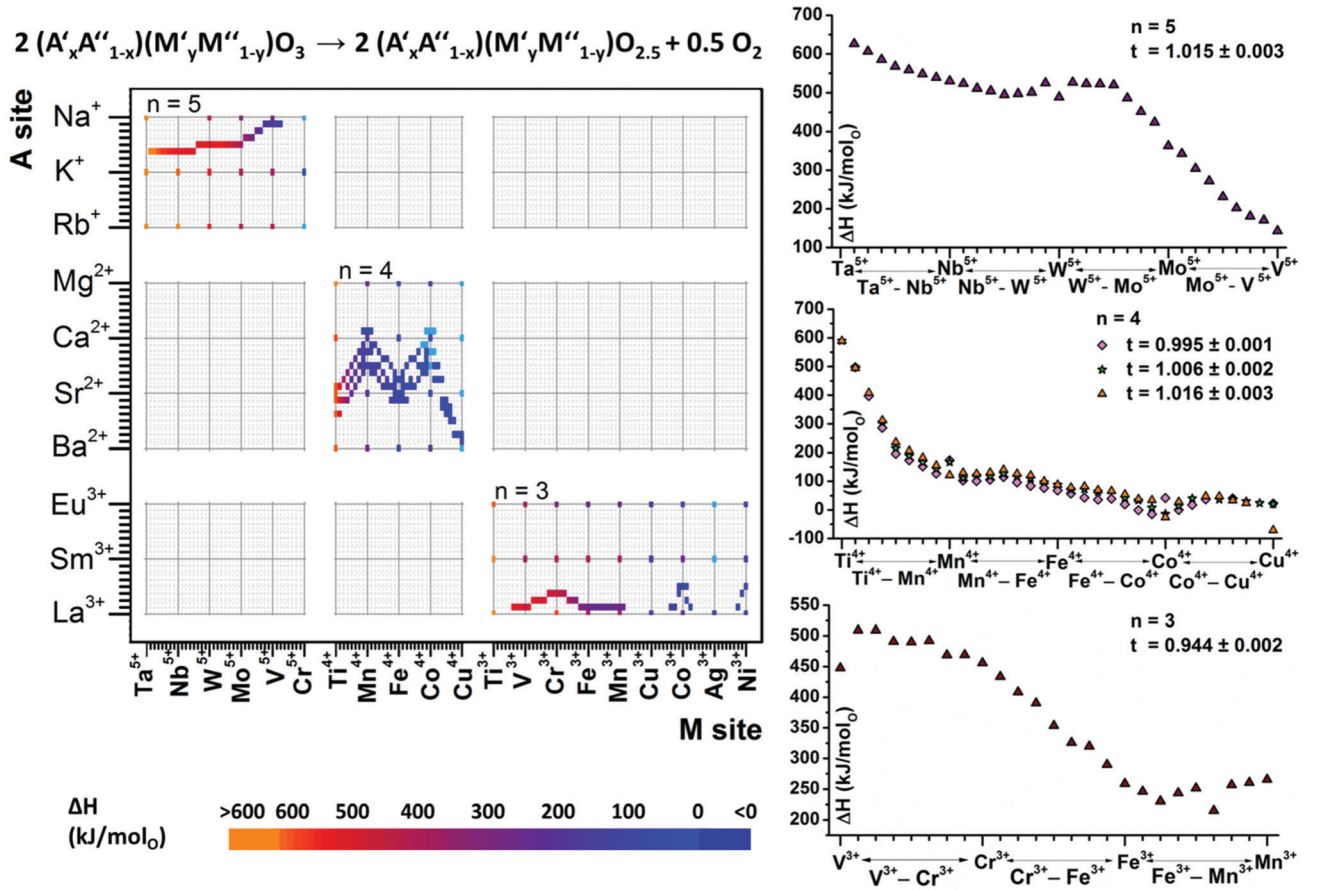

Fig. 3 Map of all >240 perovskite–brownmillerite pairs studied using DFT within this work. Each dot represents one redox pair, and its position on the *x* and *y* axis show its composition, whereas the color indicates the calculated redox enthalpy. In order to create stable solid solutions without phase transitions during redox operation, the A site composition is gradually adjusted to match different M site ionic radii. In addition to the tolerance-factor adjusted solid solutions, redox enthalpies of the solid solution endmembers are calculated, indicated by the dots at the intercepts between *x* and *y* grid lines. Right: Some selected tolerance-factor adjusted solid solution ranges with different *n* values and their redox enthalpies *vs.* different M site compositions. By solid solution formation, a large range of redox enthalpy values is covered.

of concentration have been experimentally reported for other perovskite solid solutions, where it was rationalized by different oxygen vacancy formation energetics in two chemically different environments.[63] In the calculations, the ordering of the ions is determined by minimizing the Ewald sum for a limited number of configurations which favors unit cells with uniform distribution of Ti^{4+} and Mn^{4+}. Hence, *e.g.* short-range ordering of oxygen vacancies would not be included, however, different oxygen vacancy–cation interactions are expected from the chemical difference between Mn and Ti. We note that by ordering and discretizing these unit cells to perform the DFT calculations, only one out of many possible arrangements of atoms in the lattice is considered. This ordered structure may not be energetically equivalent to the randomly disordered solid solution phase, and higher accuracy may be achieved in future studies by using special quasirandom structures (SQS),[64] or by modelling different defect-ordered and long range ordered structures and selecting the one with the lowest ground state energy for the redox enthalpy calculations. While the redox enthalpy describes the energetics of the reduction from perovskite to brownmillerite phases, this value provides no information about the absolute thermodynamic stability of each of the involved phases with respect to decomposition. In contrast, the energy above convex hull (E_{hull}) compares the formation enthalpies of the calculated phases to all other phases in the same phase space. According to E_{hull} generated through the Materials Project, the perovskite solid solutions are metastable in many cases. Nevertheless, many of these phases can be prepared successfully and do not decompose notably, as we see later. The E_{hull}, however, can be used as an indicator for the absolute stability of such perovskite phases. For instance, the E_{hull} for $Sr_7CaMnFe_7O_{24}$ is rather low at 13 meV per atom, as opposed to phases like $K_4Na_4Mo_7WO_{20}$ with a significantly higher E_{hull} = 215 meV per atom, indicating stronger tendency towards decomposition. As a guide, <25 meV per atom is often quoted as a reasonable limit for expected stability[65] while notably 10% of all experimentally observed binary oxides exhibit calculated E_{hull} > 94 meV per atom.[55] Hence, no materials in the screening are excluded based on E_{hull}, but caution should be employed as larger values (>100 meV per atom) may indicate structural instability. Future studies could elucidate which cut-off energy should be used based on the amorphous limit.[66] Moreover, the type of discretization and ordering applied may

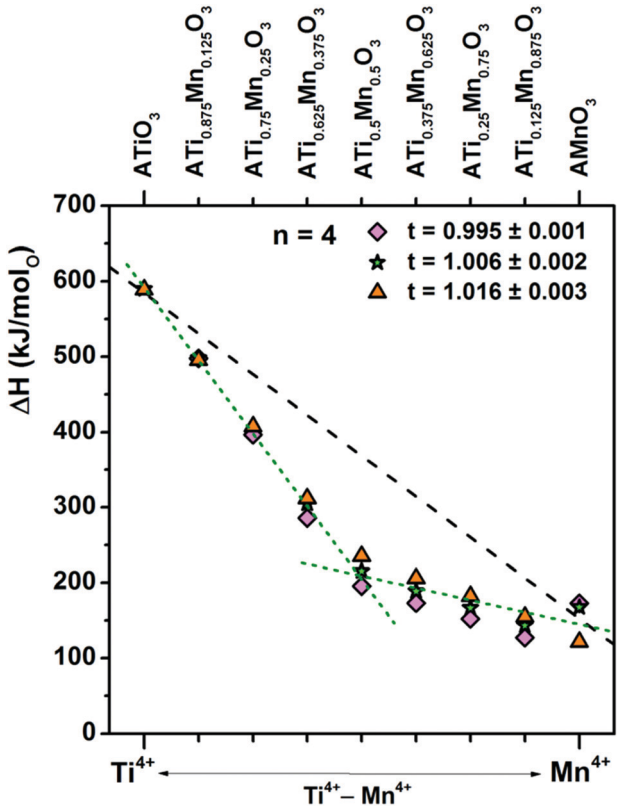

Fig. 4 Redox enthalpy of solid solutions in the exemplar Ti–Mn system with $n = 4$ for the complete reduction from perovskite to brownmillerite. The black dashed line indicates the expected redox enthalpy ΔH in terms of kJ mol_O^{-1} if it is assumed that the change in redox enthalpy is proportional to the Ti^{4+} concentration. The green dashed lines indicate the observed change in redox enthalpy showing two distinct regimes. The DFT data is shown for different tolerance factor values (t) calculated for the oxidized phase. A change in tolerance factor does not have a strong effect on the redox enthalpies, especially at high Ti^{4+} concentrations.

bias the result. Finally, the thermodynamic properties are not the only factor to consider in the materials selection process. Physical and chemical properties such as melting points and the bond polarization should not be neglected. For instance, tungsten and molybdenum bronzes (*i.e.* mixed oxides with alkali metals) show a non-stoichiometry on the A site with some phases exhibiting low melting points,[59,67] and $NaVO_3$ crystallizes with isolated vanadate cluster ions as a low-melting sodium metavanadate salt instead of forming a perovskite.[68] Although potentially stable perovskites such as $NaMoO_3$ have been identified as potential water splitting materials in earlier theoretical studies,[69] they may be impractical to apply in a real reactor due to their potentially low melting points. For these reasons, and in order to obtain a deeper understanding of the redox thermodynamics of perovskite solid solutions, it is important to combine theoretical and experimental data in our screening, as we demonstrate in the following.

Experimental materials screening

The experimental set includes perovskite solid solutions with $n = 4$ and M site solid solutions in the Ti–Mn, Mn–Fe, and Fe–Co systems. All of the 24 materials showed a pure perovskite composition as confirmed by X-ray diffraction with cubic and orthorhombic phases as expected (see the ESI†). Despite the calculated metastability of many compounds synthesized within this work, all of the experimentally synthesized compounds were formed as pure phases without side products. The compounds also remained stable within several days of redox testing in the thermobalance, as long as they were not reduced below $\delta = 0.5$ (which may lead to decomposition of Fe–Co samples under these conditions). By attempting to synthesize $EuFeO_{3-\delta}$ (calculated $t = 0.907$) and $EuCuO_{3-\delta}$ (calculated $t = 0.879$), the assumed stability limit of $t \approx 0.9$ has been confirmed: $EuFeO_{3-\delta}$ could be prepared as a single phase, whereas the "$EuCuO_{3-\delta}$" batch yielded a crude mixture of Eu_2CuO_4, Eu_2O_3, and CuO according to XRD analysis.[70]

The redox enthalpy and entropy change of the stable perovskite phases is measured as a function of the non-stoichiometry change $\Delta\delta$ with respect to a reference state $\Delta\delta_0$ with $\Delta\delta = 0$ at 400 °C and 0.18 bar oxygen partial pressure and $\Delta\delta = \delta - \delta_0$. The δ_0 values as obtained from a fit of the experimental thermodynamic data are listed in the ESI.†

For all phases studied experimentally, the stoichiometry is discretized by factors of 1/8 to compare to the corresponding theoretical phases. The average of the experimentally determined $\Delta H(\delta)$ values is compared to the DFT-calculated ΔH in Fig. 5 for each set of materials. We find a very good agreement between the experimental and theoretical enthalpy values for simple perovskites with just one M species such as $SrFeO_{3-\delta}$ and $CaMnO_{3-\delta}$ (exp. value for $CaMnO_{3-\delta}$ taken from an earlier publication by the authors, as this material was not part of this study[38]). The values are on average also in good agreement for materials with medium redox enthalpy, although significant fluctuations occur. For materials with high theoretical redox enthalpies such as for Ti-rich compounds in the Ti–Mn system, the experimental redox enthalpy values are significantly lower than those calculated using DFT. The reason for the observed inaccuracies is that only a fraction of the total range of $\delta = 0...0.5$ is covered experimentally. Especially in the case of Ti–Mn solid solutions, the samples are not reduced far enough to achieve a substantial reduction of the Ti^{4+} species, and the experimentally determined redox enthalpy refers to the reduction of the Mn^{4+} sub-lattice only. This explains the strong deviation between the average experimental ΔH values and the calculated ΔH_{DFT} for Ti-rich species, for instance in the case of $Ca_{0.375}Sr_{0.625}Ti_{0.625}Mn_{0.375}O_3$ at the rightmost of Fig. 5. To obtain a better agreement between experimental and theoretical data, we therefore introduce a model in the following describing the redox enthalpy and entropy change for perovskite solid solutions as a function of the non-stoichiometry δ.

Thermodynamics as a function of the non-stoichiometry δ

A solid solution of the type $\left(A'_xA''_{1-x}\right)\left(M'_yM''_{1-y}\right)O_3$ can be described as an ideal mixture of four pure perovskite species, *i.e.* for $Sr_{0.3}Ca_{0.7}Mn_{0.4}Fe_{0.6}O_3$:

$$\begin{array}{lll} SrMnO_3 \searrow & & \swarrow SrFeO_3 \\ & Sr_{0.3}Ca_{0.7}Mn_{0.4}Fe_{0.6}O_3 & \\ CaMnO_3 \nearrow & & \nwarrow CaFeO_3 \end{array} \quad (3)$$

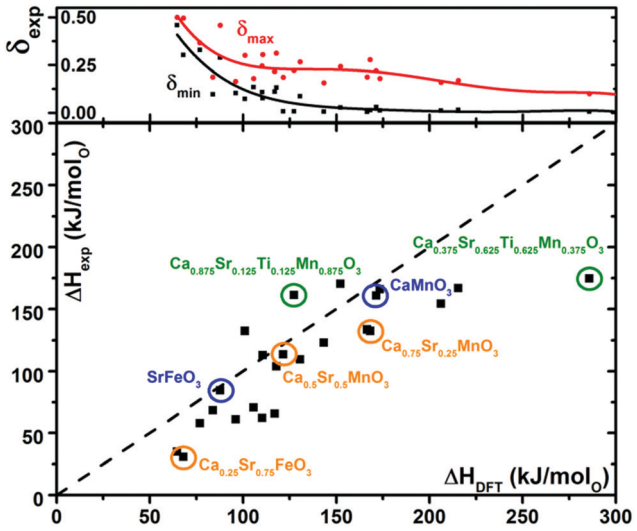

Fig. 5 Comparison of redox enthalpy values based on DFT to the experimentally determined values (exp) in terms of kJ mol^{-1} of O with some exemplary phases marked (blue: simple ternary perovskites, orange: solid solutions with only one M species, green: solid solution with two M species). The dashed line shows where the experimental and DFT values are equal.

Especially in the case of Mn–Fe solid solutions, we observe that the redox enthalpy change ΔH is dependent on $\Delta\delta$, which is typically not the case for perovskites with only one species on the M site,[38] and supports earlier results for the $SrFeO_{3-\delta}$–$SrMnO_{3-\delta}$ system.[25] This behavior is rationalized by assuming that one of the two species in the solid solution is reduced preferentially, which, in the case of the Mn–Fe system indicates that Fe^{4+} is reduced more readily than Mn^{4+}. The observed amounts of oxygen released during the reduction of such solid solutions cannot be explained solely by the reduction of Fe^{4+} to Fe^{3+} or Mn^{4+} to Mn^{3+}. Therefore, we conclude that the thermodynamics for small values of δ are governed by the reduction of Fe^{4+} with lower redox enthalpies, whereas the redox enthalpy change increases if mostly Mn^{4+} is reduced at higher δ values where most of the Fe is already in the oxidation state +3. In the intermediate region, both species contribute significantly and ΔH gradually increases with increasing δ. We model this behavior by deriving minimum and maximum values for the enthalpy change ΔH, which we call ΔH_{min} and ΔH_{max}. As an approximation, we assume individual and independent sub-lattices in the perovskite solid solution. In our example, ΔH_{min} corresponds to the oxygen vacancy formation energy of the $AFeO_3$ sub-lattice, whereas ΔH_{max} describes the oxygen vacancy formation energy of the $AMnO_3$ sub-lattice. The choice of A metal species typically only exhibits a small influence on the reaction enthalpies, which is independent of δ as these species are not involved in the redox reaction. Therefore, we use a weighted average of the reaction enthalpies of the endmembers containing the same M species. In the example (eqn (3)), we obtain

$$\Delta H_{min} = 0.3\cdot\Delta H_{SrFeO_3} + 0.7\cdot\Delta H_{CaFeO_3} \quad (4)$$

$$\Delta H_{max} = 0.3\cdot\Delta H_{SrMnO_3} + 0.7\cdot\Delta H_{CaMnO_3} \quad (5)$$

where dH_{AMO_3} refers to the DFT-based redox enthalpies for the reduction of AMO_3 to the brownmillerite $AMO_{2.5}$. The total redox enthalpy for this perovskite solid solution from perovskite to brownmillerite is then be calculated as:

$$\Delta H_{(A'_xA''_{1-x})(M'_yM''_{1-y})O_3} = \Delta H_{min}\cdot act + \Delta H_{max}\cdot(1-act) = \Delta H_{endmembers} \quad (6)$$

act refers to the stoichiometric content of M′ as the more redox active species. We denote the redox enthalpy value obtained by using weighted averages of the endmembers by $\Delta H_{endmembers}$. These values correspond to the black dashed line in Fig. 4, which indicates the linear trend. However, the actual redox enthalpy of the solid solution from perovskite to brownmillerite which is calculated using DFT (ΔH_{DFT}) may deviate from this value, as the solid solution does not necessarily act like the sum of its constituents. Therefore, we correct the values for ΔH_{min} and ΔH_{max} by the difference between this $\Delta H_{endmembers}$ and ΔH_{DFT}:

$$\Delta H_{min,corr} = \Delta H_{min} + (\Delta H_{DFT} - \Delta H_{endmembers}) \quad (7)$$

$$\Delta H_{max,corr} = \Delta H_{max} + (\Delta H_{DFT} - \Delta H_{endmembers}) \quad (8)$$

If these corrected values are applied in eqn (6), the resulting mean ΔH is equal to ΔH_{DFT}. However, this method may lead to unphysical results in some cases where the difference between the DFT value and the endmember-based value is large. For instance, if ΔH_{DFT} is significantly lower than $\Delta H_{endmembers}$ such as in the case of Ti–Mn solid solutions with $n = 4$ (see Fig. 4), $\Delta H_{min,corr}$ may even reach negative values, which means that the fully oxidized state can never be reached. This contradicts the experimental findings. Hence, we define a cutoff value of 30 kJ mol^{-1} for $\Delta H_{DFT} - \Delta H_{endmembers}$. If the difference between those two ΔH values exceeds the cutoff value, we use $\Delta H_{min} = \Delta H_{DFT} = \Delta H_{max}$ instead of eqn (7) and (8). The endmember perovskite phases, their redox enthalpies for the reduction to the brownmillerite, and the used values for ΔH_{min} and ΔH_{max} are listed in the ESI.†

We now defined limiting values ΔH_{min} and ΔH_{max} for $\delta \to 0$ and $\delta \to 0.5$, respectively. The transition between these extreme values is gradual. Using our experimental data, we empirically found that this transition between both regimes is in many cases fitted accurately using an arctangent function as explained in the ESI.† Therefore, we use this arctangent function to fit ΔH_{min} and ΔH_{max} based on our experimental data and to determine $\Delta H(\delta)$ based on this data. To determine $\Delta H(\delta,T)$ based on DFT data, however, we need to derive a model for the contributions of the two individual sub-lattices to the total oxygen non-stoichiometry δ. The total non-stoichiometry as a function of the temperature T and the oxygen partial pressure p_{O_2} in an ideal solid solution of two perovskites is the sum of the non-stoichiometries induced in both individual sub-lattices. Based on basic thermodynamics, we calculate the oxygen non-stoichiometry in both individual sub-lattices and derive an expression for the oxygen partial pressure of the system $p_{O_2}(\delta, \Delta H_{min}, \Delta H_{max}, T)$. $\Delta H(\delta,T)$ is then calculated as a numerical derivative of p_{O_2} with respect to the temperature. This model is

explained in greater detail in the ESI.† Within this model, the steepness of the increase from ΔH_{min} to ΔH_{max} is temperature dependent. At very low temperatures (*i.e.* 73 K), $\Delta H(\delta)$ resembles a step function, whereas at higher temperatures (*i.e.* 573 K), it is very similar to the arctangent function used for the experimental data. The reason why we cannot use our theoretical expressions to also fit the experimental data is that we do not have a bijective relation between measured values of $\delta - \Delta H$ datasets and the temperature (that means, one $\Delta H(\delta)$ value was measured at multiple temperature levels). As noted in the Experimental section, measuring $\Delta H(\delta,T)$ would require much longer measurement times, which are not feasible within the framework of a large materials screening. Moreover, the numerical solution presented here leads to a very slow fitting process.

The redox entropy change ΔS upon non-stoichiometric reduction of a perovskite can be calculated as the sum of the partial molar entropy of oxygen $S_{O_2}(T)$, the vibrational entropy change $\Delta s_{vib}(T)$, and the configurational entropy change $\Delta s_{conf}(\delta,T)$:[38,71,72]

$$\Delta S(\delta, T) = \frac{1}{2} S_{O_2}(T) + \Delta s_{vib}(T) + \Delta s_{conf}(\delta, T) \qquad (9)$$

The entropy change in perovskite solid solutions can be fit from experimental data as explained in the ESI.† It can, however, also be modelled based on DFT data and the literature. $S_{O_2}(T)$ can be calculated using the Shomate equation and the NIST-JANAF thermochemical tables.[73] The vibrational entropy change can be determined using the Debye model based on elastic tensors derived through DFT calculations.[74] The configurational entropy change is obtained through a dilute species model.[71] For details and the derivation of the respective equations, the interested reader is referred to the ESI.†

Using our newly derived expressions for $\Delta H(\delta,T)$, $\Delta S(\delta,T)$, and $\delta(T, p_{O_2}, \Delta H_{min}, \Delta H_{max})$, we calculate the equilibrium position for any of the perovskite solid solutions in the DFT dataset and compare it to the corresponding experimental data. Using the *RedoxThermoCSP* app created by the authors, isographs are drawn for each of the materials. As an example, we consider the solid solution $Ca_{0.25}Sr_{0.75}Mn_{0.625}Fe_{0.375}O_{3-\delta}$. Fig. 6 shows three of the isographs created with *RedoxThermoCSP* user interface. Within the window of experimentally measured data, the experimental and theoretical data are in good agreement. At low temperatures, deviations occur which are attributed to the temperature dependence of the entropy change, which is not accounted for in simple experimental fit equations.

If we look at the simple reference case of $SrFeO_{3-\delta}$ with well-known redox properties (see the *RedoxThermoCSP* interface),[22,25,42] the theoretical model often leads to an overestimated redox enthalpy and entropy change, which in most cases causes the prediction of higher reduction temperatures than measured experimentally. Our theoretical model predicts an increased redox enthalpy with increasing temperature, however the increase may be overestimated. Moreover, the real redox entropy may be lower than in our model due to a lower change in configurational entropy associated with oxygen vacancy ordering.[39] We do not account for vacancy ordering in our model, but future DFT studies could include vacancy-ordered phases. Identifying the most stable

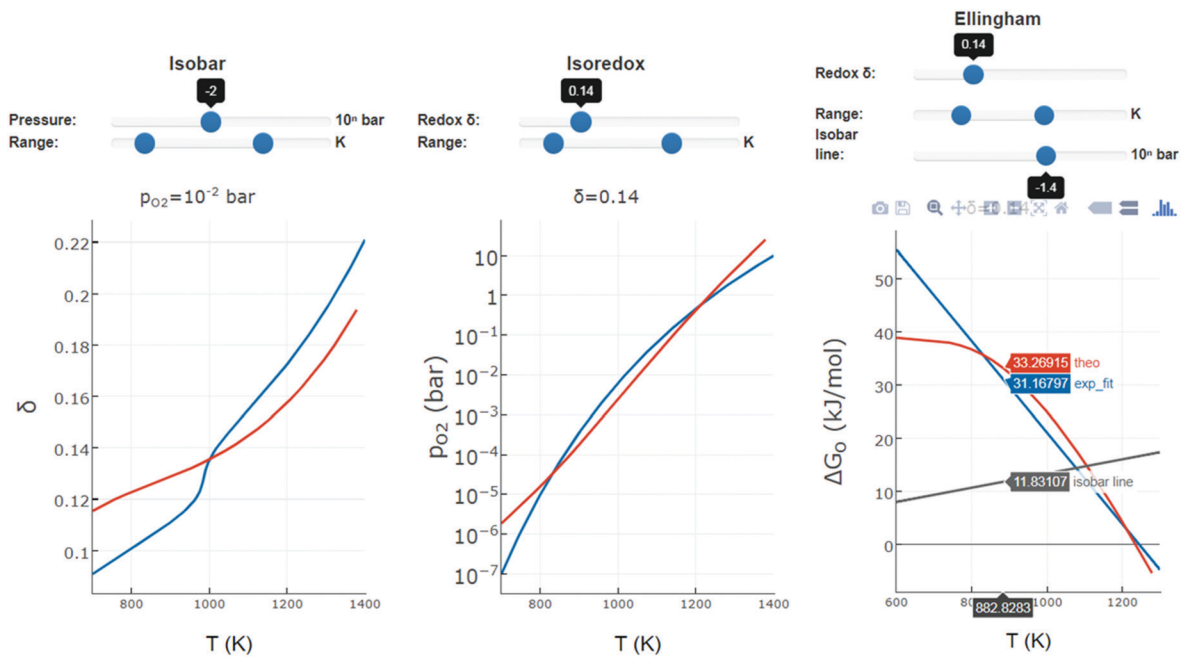

Fig. 6 Exemplary isograph plots of the user interface "RedoxThermoCSP" for the exemplary solid solution $Ca_{0.25}Sr_{0.75}Mn_{0.625}Fe_{0.375}O_{3-\delta}$ with a comparison between experimental data (blue) and theoretical data (red). All graphs are interactive, meaning that the user can define values using the sliders above the graphs, read values by hovering over the graph (see the graph on the right), and download the graph and its data. Left: The isobar for $p_{O_2} = 10^{-2}$ bar shows the non-stoichiometry in the perovskite lattice as a function of the temperature. Extrapolated experimental data is shown as dashed line, whereas data from the experimental fit is shown as solid line. Middle: The isoredox plot shows the predicted equilibrium oxygen partial pressure for different temperatures and a constant value δ = 0.14. Right: The Gibbs free energy ΔG for a constant δ = 0.14 is shown in an Ellingham diagram.

vacancy-ordered phase, however, is beyond the scope of this work, as it requires a cluster-expansion for each chemical environment. Furthermore, we do not consider enthalpy–entropy compensation effects in our models. The enthalpy and entropy change cannot be experimentally determined independently from each other,[58] which means that that experimental ΔH and ΔS data may exhibit inaccuracies, while the ΔG should be unaffected. Moreover, the experimentally-determined value of δ_0 as calculated through entropy fits (see ESI†) is susceptible to inaccuracies in the measured data. For this reason, some datasets (for instance: $Ca_{0.25}Sr_{0.75}Fe_{0.625}Co_{0.375}O_{3-\delta}$) show a constant offset between the absolute δ values in the experimental and theoretical datasets. Despite the approximations made in our model, the release or uptake of oxygen between a certain reduction and oxidation temperature as indicated by isobars and isotherms is predicted accurately for many materials. Major discrepancies can mainly be found at low values of δ where the theoretical model predicts further oxidation, which is not observed in the real system due to kinetic limitations, as well as outside the experimentally covered data range, which is indicated in the *RedoxThermoCSP* database. All presented data is available through the *RedoxThermoCSP* user interface as a part of MPContribs.

Materials specific energy demand of perovskite redox cycles

Based on the equilibrium thermodynamics of the studied materials, we can estimate the energy demand of a perovskite-based two-step thermochemical redox cycle under different conditions. We do not assume one specific reactor design or develop reactor designs for different thermochemical applications. Studies on different reactor designs in the field of solar thermochemistry are available in the literature.[75–79] Instead, to avoid limiting the applicability of this study to one specific reactor setup, we used generic properties such as the reduction and oxidation temperatures and pressures and temperature-independent heat recovery efficiencies. If these properties are known for a specific reactor design, our work can be used to help identify ideal materials for this specific application.

As a first step, we define the conditions for reduction and oxidation. We assume that the redox material is in equilibrium at the end of the redox reaction and that only this equilibrium position is relevant for the redox energetics. At the end of the reduction process, an oxygen partial pressure p_{red} is reached at the temperature T_{red} as the released oxygen is removed from the reaction chamber. Conversely, the material is re-oxidized at T_{ox} at an equilibrium oxygen partial pressure p_{ox}. Instead of the oxygen partial pressure at oxidation, the p_{H_2}/p_{H_2O} or p_{CO_2}/p_{CO_2} partial pressure ratios can be specified if water or CO_2 are used as the respective oxidants. These ratios can be converted into equivalent oxygen partial pressures (see ESI†) assuming that the water or carbon-dioxide splitting reaction is in the equilibrium state for the given temperature and partial pressure ratio. We assume that no additional oxygen (for instance due to leakage) is present. Under these assumptions, we can define a generic process scheme for the complete thermochemical cycle. The energy balance can then be written as

$$\dot{Q}_{in} = \underbrace{\dot{Q}_{chem} + \dot{Q}_{sensible} + \dot{Q}_{pump}\left(+\dot{Q}_{steam}\right)}_{\dot{Q}_{total}} + \text{losses} \qquad (10)$$

The total energy flow used for operating the redox cycle is denoted by $\dot{Q}_{total}$. Heat losses due to heat-transfer processes are summarized as "losses". These are not further considered in the following, meaning that heat losses due to radiation, conduction, and convection are neglected in our model. This is a necessary limitation, as these factors are dependent on the reactor design and operational parameters, which cannot be generalized. We therefore only consider the total thermal energy that can be used in the redox cycle Q_{total}. Instead of the heat flow $\dot{Q}_{total}$, we use the absolute amount of thermal energy used in the process, as the exact flow rates depend on the reaction kinetics and heating rates.

The four contributions to our energy balance are derived in detail in the ESI.† For brevity, we summarize the resulting equations in the following. The "chemical energy" Q_{chem} refers to the amount of energy required to drive the chemical reaction, *i.e.*, the reduction and re-oxidation of the redox material. Within one redox cycle, its magnitude can be decreased if the heat released during oxidation is partially re-used for the next reduction cycle using solid–solid heat exchangers with the efficiency $\eta_{hrec,solid}$. Moreover, in the case of water splitting and CO_2 splitting, the energy stored in the reaction products H_2 or CO_2 needs to be taken into account by considering the temperature-dependent reaction enthalpies of water and CO_2 splitting ($\Delta H_{stored}(T)$).

$$Q_{chem} = \left(1 - \eta_{hrec,solid}\right) \cdot \int_{\delta_{ox}}^{\delta_{red}} \Delta H(\delta, T)\, \mathrm{d}\delta - \Delta H_{stored}(T)$$
$$\eta_{hrec,solid} = 0 \ldots 1 \qquad (11)$$

The "sensible energy" $Q_{sensible}$ is dependent on the latent heat stored in the material based on its heat capacity, which can be calculated using the Debye model. Using DFT and *pymatgen*, the Debye temperatures of the perovskite (δ = 0) and brownmillerite phases (δ = 0.5) can be determined using their elastic tensors.[48,74] The contribution of the sensible energy to the total energy demand per mole of redox material can then be determined by integration over the heat capacity between T_{ox} and T_{red}:

$$Q_{sensible} = \int_{T_{ox}}^{T_{red}} C(T, \delta_{ox}, \delta_{red})\mathrm{d}T \cdot \left(1 - \eta_{hrec,solid}\right) \qquad (12)$$

In analogy to the chemical energy input, the sensible energy input per redox cycle can be lowered if the heat released during cool down is recovered, which is expressed by the heat recovery efficiency $\eta_{hrec,solid}$.

The third component of the energy input, the "pumping energy" Q_{pump}, describes the energy required to lower the oxygen partial pressure during the reduction step. We assume that this energy cannot be recovered and is always supplied as thermal energy, which is converted into electrical energy for mechanical pumps at an assumed efficiency of 40%. One can use a function to estimate the pumping energy if mechanical pumps are used. Brendelberger *et al.* developed an envelope function describing the minimum energy input necessary for mechanical pumping, which is used within this work (see ESI†).[80]

For water-splitting cycles, the energy required to generate steam as an oxidant should not be neglected ("steam-generation energy", Q_{steam}). Some materials may split water at a low energy

input but also at low conversion rates. Thus, a large amount of water would have to be heated and evaporated to obtain a reasonable amount of hydrogen. The steam-generation energy can be calculated as follows:

$$Q_{\text{steam}}{}' = \left(\int_{T_{\text{feed}}}^{373.15\,\text{K}} C_{\text{p,water}}\,\mathrm{d}T + \Delta H_{\text{vap}} + \int_{373.15\text{K}}^{0.5(T_{\text{ox}}+T_{\text{red}})} C_{\text{p,steam}}\,\mathrm{d}T \right) \times \left(1 - \eta_{\text{hrec,steam}}\right) \quad (13)$$

Part of the energy supplied may be recovered from the steam/gas mixture leaving the reactor using a heat exchanger at a heat-recovery efficiency $\eta_{\text{hrec,steam}}$. The calculated energy demand is given per mole of water. To determine the energy demand per mole of hydrogen produced, we need to divide the resulting value by the target partial pressure ratio of hydrogen *vs.* water $p(H_2)/p(H_2O)$:

$$Q_{\text{steam}} = \frac{Q_{\text{steam}}{}'}{p(\text{H}_2)/p(\text{H}_2\text{O})} \quad (14)$$

This concludes the list of material- and process-specific energy penalties required in order to account for in a two-step (solar) thermochemical redox cycle. Based on this data, we created a perovskite search engine as part of *MPContribs*.‡ Users can define process parameters such as the reduction and oxidation oxygen partial pressure and temperature, the heat recovery efficiency, and, for water splitting, the target $p(H_2)/p(H_2O)$ and the water feed temperature.

As an example, we look at a thermochemical air separation process with reduction at 1000 °C in air and oxidation at 500 °C and $p_{O_2} = 10^{-6}$ bar to prepare nitrogen for the Haber–Bosch process.[81–83] The energy analysis for such a cycle based on theoretical data is shown in Fig. 7 with an assumed solid–solid heat-recovery efficiency of 60%. The materials with the lowest energy demand include mainly calcium strontium manganates in solid solution with iron- or titanium-containing perovskites. The material with the lowest calculated energy demand is $Sr_{0.875}Ba_{0.125}Fe_{0.75}Co_{0.25}O_{3-\delta}$, as it is predicted to undergo a large mass change under these conditions. This material can be seen as a partially cobalt-substituted analogue to $SrFeO_{3-\delta}$ with lower redox enthalpy (81.8 *vs.* 87.8 kJ mol_O^{-1} for complete reduction from $\delta = 0$ to $\delta = 0.5$). $SrFeO_{3-\delta}$ has been introduced as a suitable material for solar-thermochemical air separation in the literature,[22,84,85] and our work offers the chance to find doped variants with adjusted thermodynamics for specific redox conditions. It has been shown in the literature that cobalt-containing perovskites are reduced readily and therefore are suitable oxygen carriers in thermochemical air separation processes.[86] Partial cobalt substitution allows lowering the redox enthalpy in $SrFeO_{3-\delta}$-based perovskites. Another material with favorable thermodynamics in our study is $LaNiO_{3-\delta}$ (No. 2 in Fig. 7). Literature reports on the redox properties of this material are scarce; however, Ni^{3+} has been shown to be relatively easily reduced to Ni^{2+} in this phase.[87]

Interestingly, the total amount of energy required to pump one mole of oxygen using the most efficient materials is usually on the same order of magnitude, irrespective of the redox temperature and partial pressure levels. The most efficient materials always show large changes in δ under the conditions applied, and as δ is limited, the largest achievable values for $\Delta\delta$

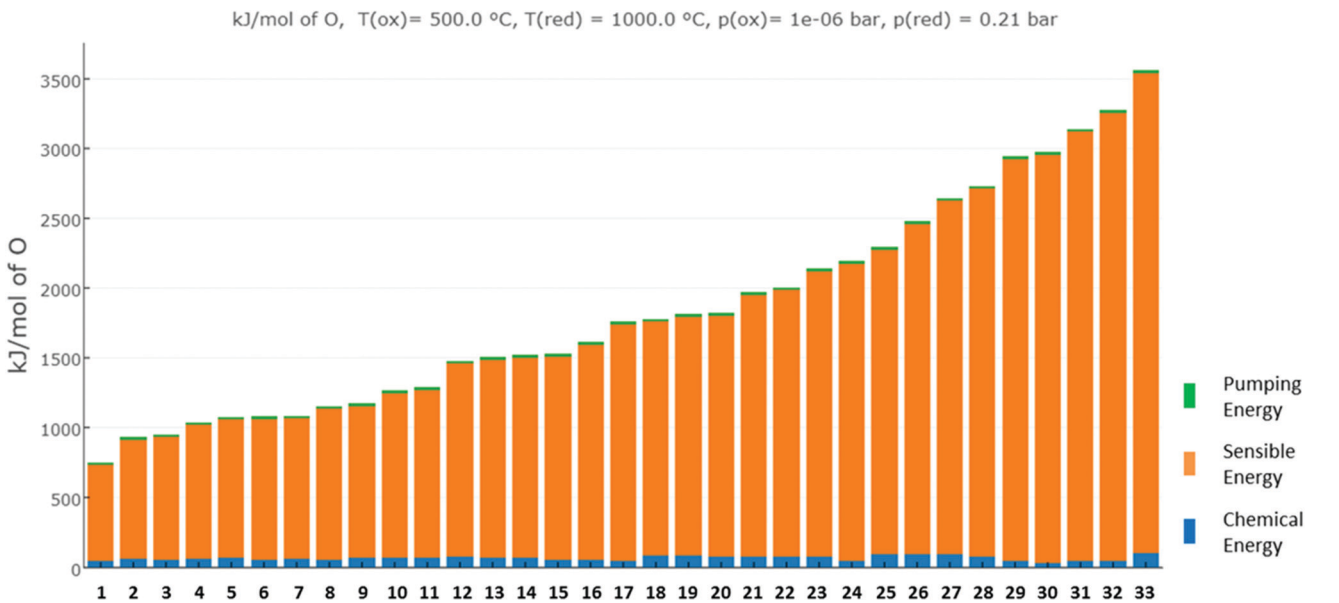

Fig. 7 Data from *RedoxThermoCSP* showing a ranked list of perovskite materials based on theoretical data for an air-separation process operated between 500 °C and 1000 °C at 10^{-6}/0.21 bar oxygen partial pressure under the assumption of $\eta_{\text{hrec,solid}} = 0.6$. The chemical energy and pumping energy demands are low compared with the sensible energy input. The materials associated with the lowest energy consumption are $Sr_{0.875}Ba_{0.125}Fe_{0.75}Co_{0.25}O_{3-\delta}$ and $LaNiO_{3-\delta}$. Only the 33 materials with the lowest energy consumption per cycle out of >240 materials are shown. The material compositions were replaced by indexes for clarity; see the *RedoxThermoCSP* interface for the corresponding compositions.

are always in a similar range (typically $\Delta\delta$ = 0.1–0.3). As the sensible energy input per mole of O is inversely proportional to $\Delta\delta$, this value for the most efficient materials is consequently also similar in many cases. The materials at the end of our ranked list are associated with such small changes in δ under the set conditions that several tons of material would be required to transfer even a small amount of oxygen, resulting in their high sensible energy demand per mole of O. Compared with the sensible energy demand, the chemical and pumping energy only contribute a small portion to the total energy demand in our exemplary case.

Details on an analysis for a water splitting cycle can be found in the ESI.† In summary, we show a large set of potential water splitting materials and demonstrate how perovskites can be used to efficiently split water at low reduction temperatures and conversion rates. As shown in the literature, many perovskites require heating a large excess of steam which often outweighs their advantages in terms of lower reduction temperatures *vs.* the current state-of-the-art material ceria and leads to an overall lower heat-to-fuel efficiency.[88] Nevertheless, our data shows that based on our model, there are some perovskites which can be used at low reduction temperatures and moderate steam excess ratios, which allow reaching heat-to-fuel efficiencies of perovskite-based cycles at 1300–1350 °C which are comparable to those for ceria at 1450–1500 °C. At 1300 °C, our perovskites show up to 50% higher heat-to-fuel efficiency values than ceria. The absolute efficiency values discussed in the ESI† of only a few percent appear discouraging at first, but can be substantially increased when improving heat recovery and oxygen pumping. One also has to state that our model, which assumes chemical equilibrium, is highly simplified.[89,90] Our tool is a good means of comparing materials relative to each other and coarsely estimating the total energy penalty, but cannot replace an in-depth model of the reactor-specific conversion extent and equilibrium state. All in all, we can conclude that lowering the reduction temperature using perovskites instead of ceria while maintaining the same heat-to-fuel efficiency is an attractive option for mitigating the engineering challenges associated with reactors at very high temperatures.

Despite materials-specific aspects, it is also important to consider the economics of such redox cycles. Choosing materials with a substantial rare earth metal content is only reasonable if the required amount of redox material is small and if it offers a significant advantage in efficiency over perovskites with earth-abundant metals such as $SrFeO_{3-\delta}$. Moreover, the chemical stability and toxicity of the materials have to be considered. Our perovskite search engine is therefore designed as a materials pre-selection tool, which reduces the amount of materials to consider in the selection process. Depending on the specific operating conditions of the redox cycle, not all of the materials shown in our lists are suitable. Moreover, the accuracy of our data can be improved if the amount of materials to be screened is reduced by using more accurate representations of the solid solutions for DFT calculations and performing a larger amount of experimental tests, as discussed in the ESI.† Nevertheless, our data can be used to predict the redox properties of a large set of perovskite materials well enough to significantly narrow down the list of potential materials.

Conclusions

In this work, we introduced a novel method of designing perovskite solid solutions for two-step thermochemical redox cycles. Based upon the different redox potentials of different transition metal species, we select two species and create $AMO_{3-\delta}$ perovskites with mixed M site occupancy (solid solutions). To adjust for the different ionic radii of different transition metal species, we select the charge-balancing A cations accordingly to maintain a constant tolerance factor by mixing two different species on the A site. The results are metal oxide solid solutions which are reduced and re-oxidized non-stoichiometrically without change of the crystal system while introducing oxygen vacancies with $\delta = 0...0.5$. For the first time, we offer a method to rationally design these perovskite solid solutions in a broad range of enthalpies from −340 to 706 kJ per mol of oxygen (kJ mol_O^{-1}) for the reduction of a perovskite with δ = 0 to a brownmillerite with δ = 0.5.

In the case of a mixed M site occupancy, the redox enthalpy and entropy change are dependent on the oxygen non-stoichiometry δ. We develop a model describing the change in ΔH and ΔS dependent on δ based on fundamental thermodynamics and using DFT-computed redox enthalpies and elastic tensors. The generated expressions for $\Delta H(\delta)$ and $\Delta S(\delta)$ are then used to calculate the equilibrium state of the perovskite solid solutions depending on the temperature and oxygen partial pressure. For about 1/10 of the materials studied theoretically, we performed experimental tests to validate the theoretical model, and fit experimentally determined thermodynamic data using an empirical model. While the theoretical model can still be improved by predicting changes in the thermodynamic properties due to oxygen vacancy ordering, we generally found a good agreement between the predicted changes in non-stoichiometry and the experimental values.

As our thermodynamic data allows the calculation of the change in non-stoichiometry under different redox conditions, it is possible to predict the amount of O_2 released, or in the case of thermochemical fuels production, the amount of H_2 or CO generated. Moreover, the amount of energy necessary to drive such a redox cycle can be calculated, and used to rank different redox materials according to their energy consumption in a two-step thermochemical cycle for air separation, water splitting, or carbon-dioxide splitting. Our models consider the thermal energy required to drive the chemical reaction, the sensible energy stored in the redox materials at high temperature, and the energy necessary to maintain a low oxygen partial pressure during reduction through pumping. For air separation and oxygen pumping, we can identify ideally suitable materials for each range of target oxygen partial pressures. The most promising applications for this technology are processes that require very low oxygen concentrations. For water splitting, the energy necessary to generate steam is also considered. Although our work cannot

entirely replace experimental tests, it is possible to significantly limit the range of possible candidate materials based on thermodynamic parameters. All the data we gathered is freely available to the public in an interactive online resource, which allows anyone to select potentially promising perovskite materials and study the effect of different operational parameters in a solar-thermochemical redox cycle.

Conflicts of interest

There are no conflicts to declare.

Acknowledgements

The authors would like to acknowledge valuable ideas provided by Dr Joseph Montoya (Lawrence Berkeley National Laboratory) for the calculation of elastic properties and the heat capacity. This work has received funding from the Helmholtz Association within the Virtual Institute SolarSyngas (VH-VI-509) and the project DÜSOL (EFRE-0800603) which is co-funded in the Klimaschutzwettbewerb "ErneuerbareEnergien.NRW" by the state of Northrhine-Westphalia, Germany, and the European EFRE fund. The co-author L. Z. would like to acknowledge the financial support from the China Scholarships Council. Computational work was funded by the U.S. Department of Energy (DOE), Office of Science, Office of Basic Energy Sciences, Materials Sciences and Engineering Division under Contract No. DE-AC02-05-CH11231 (Materials Project program KC23MP). M. H. was also supported as part of the Computational Materials Sciences Program funded by the DOE, Office of Science, Basic Energy Sciences, Materials Sciences and Engineering Division (award no. DE-SC0014607). This research used resources of the National Energy Research Scientific Computing Center, a DOE Office of Science User Facility supported by the Office of Science of the DOE under contract no. DE-AC02-05CH1123.

Notes and references

1 A. Jain, G. Hautier, C. J. Moore, S. Ping Ong, C. C. Fischer, T. Mueller, K. A. Persson and G. Ceder, *Comput. Mater. Sci.*, 2011, **50**, 2295–2310.
2 A. Jain, J. Montoya, S. Dwaraknath, N. E. R. Zimmermann, J. Dagdelen, M. Horton, P. Huck, D. Winston, S. Cholia, S. P. Ong and K. Persson, in *Handbook of Materials Modeling: Methods: Theory and Modeling*, ed. W. Andreoni and S. Yip, Springer International Publishing, Cham, 2018, pp. 1–34.
3 A. Jain, S. P. Ong, G. Hautier, W. Chen, W. D. Richards, S. Dacek, S. Cholia, D. Gunter, D. Skinner, G. Ceder and K. A. Persson, *APL Mater.*, 2013, **1**, 011002.
4 A. Jain, Y. Shin and K. A. Persson, *Nat. Rev. Mater.*, 2016, **1**, 15004.
5 Q. Yan, J. Yu, S. K. Suram, L. Zhou, A. Shinde, P. F. Newhouse, W. Chen, G. Li, K. A. Persson, J. M. Gregoire and J. B. Neaton, *Proc. Natl. Acad. Sci. U. S. A.*, 2017, **114**, 3040–3043.
6 T. Nakamura, *Sol. Energy*, 1977, **19**, 467–475.
7 D. Marxer, P. Furler, M. Takacs and A. Steinfeld, *Energy Environ. Sci.*, 2017, **10**, 1142–1149.
8 B. Moghtaderi, *Energy Fuels*, 2010, **24**, 190–198.
9 K. Kumabe, T. Sato, K. Matsumoto, Y. Ishida and T. Hasegawa, *Fuel*, 2010, **89**, 2088–2095.
10 G. Bozzano and F. Manenti, *Prog. Energy Combust. Sci.*, 2016, **56**, 71–105.
11 C.-J. Yang and R. B. Jackson, *Energy Policy*, 2012, **41**, 878–884.
12 J. Vieten, B. Bulfin, F. Call, M. Lange, M. Schmücker, A. Francke, M. Roeb and C. Sattler, *J. Mater. Chem. A*, 2016, **4**, 13652–13659.
13 B. Bulfin, J. Vieten, C. Agrafiotis, M. Roeb and C. Sattler, *J. Mater. Chem. A*, 2017, **5**, 18951–18966.
14 M. Takacs, J. R. Scheffe and A. Steinfeld, *Phys. Chem. Chem. Phys.*, 2015, **17**, 7813–7822.
15 F. Call, M. Roeb, M. Schmücker, C. Sattler and R. Pitz-Paal, *J. Phys. Chem. C*, 2015, **119**, 6929–6938.
16 N. Knoblauch, H. Simon, L. Dörrer, D. Uxa, P. Fielitz, J. Wendelstorf, K.-H. Spitzer, M. Schmücker and G. Borchardt, *Inorganics*, 2017, **5**, 76.
17 K. Ehrensberger, A. Frei, P. Kuhn, H. R. Oswald and P. Hug, *Solid State Ionics*, 1995, **78**, 151–160.
18 C. Agrafiotis, A. Zygogianni, C. Pagkoura, M. Kostoglou and A. G. Konstandopoulos, *AIChE J.*, 2013, **59**, 1213–1225.
19 C. Ling, R. Zhang and H. Jia, *ACS Appl. Mater. Interfaces*, 2015, **7**, 14518–14527.
20 S. M. Babiniec, E. N. Coker, J. E. Miller and A. Ambrosini, *Int. J. Energy Res.*, 2016, **40**, 280–284.
21 L. Imponenti, K. J. Albrecht, R. J. Braun and G. S. Jackson, *ECS Trans.*, 2016, **72**, 11–22.
22 J. Vieten, B. Bulfin, E. Starr David, A. Hariki, M. F. de Groot Frank, A. Azarpira, C. Zachäus, M. Hävecker, K. Skorupska, N. Knoblauch, M. Schmücker, M. Roeb and C. Sattler, *Energy Technol.*, 2019, **7**, 131–139.
23 T. Ishigaki, S. Yamauchi, K. Kishio, J. Mizusaki and K. Fueki, *J. Solid State Chem.*, 1988, **73**, 179–187.
24 K. Huang, R. S. Tichy and J. B. Goodenough, *J. Am. Ceram. Soc.*, 1998, **81**, 2565–2575.
25 J. Vieten, B. Bulfin, M. Senholdt, M. Roeb, C. Sattler and M. Schmücker, *Solid State Ionics*, 2017, **308**, 149–155.
26 V. M. Goldschmidt, *Naturwissenschaften*, 1926, **14**, 477–485.
27 A. Simon, *Coord. Chem. Rev.*, 1997, **163**, 253–270.
28 G. Gou, N. Charles, J. Shi and J. M. Rondinelli, *Inorg. Chem.*, 2017, **56**, 11854–11861.
29 K. I. Kobayashi, T. Kimura, H. Sawada, K. Terakura and Y. Tokura, *Nature*, 1998, **395**, 677.
30 I. Grinberg, V. R. Cooper and A. M. Rappe, *Nature*, 2002, **419**, 909.
31 R. Shannon, *Acta Crystallogr., Sect. A: Cryst. Phys., Diffr., Theor. Gen. Crystallogr.*, 1976, **32**, 751–767.
32 Y. Kudoh, C. T. Prewitt, L. W. Finger and E. Ito, Ionic Radius-Bond Strength Systematics, Ionic Compressibilities, and an Application to (Mg, Fe)SiO_3 Perovskites, in *High-pressure Research: Application to Earth and Planetary Sciences*, Geophysical Monograph Series, 1992.
33 B. Dabrowski, O. Chmaissem, J. Mais, S. Kolesnik, J. D. Jorgensen and S. Short, *J. Solid State Chem.*, 2003, **170**, 154–164.

34 C. Chatzichristodoulou, P. Norby, P. V. Hendriksen and M. B. Mogensen, *J. Electroceram.*, 2015, **34**, 100–107.
35 A. Glazer, *Acta Crystallogr., Sect. A: Cryst. Phys., Diffr., Theor. Gen. Crystallogr.*, 1975, **31**, 756–762.
36 P. Woodward, *Acta Crystallogr., Sect. B: Struct. Sci.*, 1997, **53**, 44–66.
37 J. S. Zhou and J. B. Goodenough, *Phys. Rev. Lett.*, 2005, **94**, 065501.
38 B. Bulfin, J. Vieten, D. E. Starr, A. Azarpira, C. Zachäus, M. Haevecker, K. Skorupska, M. Schmücker, M. Roeb and C. Sattler, *J. Mater. Chem. A*, 2017, **5**, 7912–7919.
39 M. Schmidt and S. J. Campbell, *J. Phys. Chem. Solids*, 2002, **63**, 2085–2092.
40 X. Liu, R. Hong and C. Tian, *J. Mater. Sci.: Mater. Electron.*, 2008, **20**, 323–327.
41 A. Jain, G. Hautier, S. P. Ong, C. J. Moore, C. C. Fischer, K. A. Persson and G. Ceder, *Phys. Rev. B: Condens. Matter Mater. Phys.*, 2011, **84**, 045115.
42 Y. Takeda, K. Kanno, T. Takada, O. Yamamoto, M. Takano, N. Nakayama and Y. Bando, *J. Solid State Chem.*, 1986, **63**, 237–249.
43 A. R. Oganov and S. Ono, *Nature*, 2004, **430**, 445.
44 M. Laing, *J. Chem. Educ.*, 2009, **86**, 188.
45 M. Ezbiri, M. Takacs, D. Theiler, R. Michalsky and A. Steinfeld, *J. Mater. Chem. A*, 2017, **5**, 4172–4182.
46 T. Cooper, J. R. Scheffe, M. E. Galvez, R. Jacot, G. Patzke and A. Steinfeld, *Energy Technol.*, 2015, **3**, 1130–1142.
47 S. P. Jiang, *J. Mater. Sci.*, 2008, **43**, 6799–6833.
48 S. P. Ong, W. D. Richards, A. Jain, G. Hautier, M. Kocher, S. Cholia, D. Gunter, V. L. Chevrier, K. A. Persson and G. Ceder, *Comput. Mater. Sci.*, 2013, **68**, 314–319.
49 K. Mathew, J. H. Montoya, A. Faghaninia, S. Dwarakanath, M. Aykol, H. Tang, I.-H. Chu, T. Smidt, B. Bocklund, M. Horton, J. Dagdelen, B. Wood, Z.-K. Liu, J. Neaton, S. P. Ong, K. Persson and A. Jain, *Comput. Mater. Sci.*, 2017, **139**, 140–152.
50 G. Kresse and J. Furthmüller, *Phys. Rev. B: Condens. Matter Mater. Phys.*, 1996, **54**, 11169–11186.
51 G. Kresse and J. Furthmüller, *Comput. Mater. Sci.*, 1996, **6**, 15–50.
52 A. Jain, S. P. Ong, W. Chen, B. Medasani, X. Qu, M. Kocher, M. Brafman, G. Petretto, G.-M. Rignanese, G. Hautier, D. Gunter and K. A. Persson, *Concurr. Comp.: Pract. Exper.*, 2015, **27**, 5037–5059.
53 D. C. Langreth and M. J. Mehl, *Phys. Rev. B: Condens. Matter Mater. Phys.*, 1983, **28**, 1809–1834.
54 J. P. Perdew, K. Burke and M. Ernzerhof, *Phys. Rev. Lett.*, 1996, **77**, 3865–3868.
55 W. Sun, S. T. Dacek, S. P. Ong, G. Hautier, A. Jain, W. D. Richards, A. C. Gamst, K. A. Persson and G. Ceder, *Sci. Adv.*, 2016, **2**, e1600225.
56 J. Vieten and K. A. Persson, *Materials Project DOI Collection*, 2018, DOI: 10.17188/1475589.
57 J. Vieten, B. Bulfin, M. Roeb and C. Sattler, *Solid State Ionics*, 2018, **315**, 92–97.
58 R. R. Krug, W. G. Hunter and R. A. Grieger, *Nature*, 1976, **261**, 566.
59 E. Kazuo, F. Kouichi, H. Fumikazu, T. Sadao and S. Noriyuki, *Bull. Chem. Soc. Jpn.*, 1991, **64**, 161–164.
60 L. Vegard, *Z. Phys.*, 1921, **5**, 17–26.
61 S. Darracq, S. G. Kang, J. H. Choy and G. Demazeau, *J. Solid State Chem.*, 1995, **114**, 88–94.
62 X. J. Wu, P. Laffez, H. Yamauchi and N. Môri, *Phys. C*, 1994, **228**, 292–298.
63 J. Cheng, A. Navrotsky, X.-D. Zhou and H. U. Anderson, *Chem. Mater.*, 2005, **17**, 2197–2207.
64 A. van de Walle, P. Tiwary, M. de Jong, D. L. Olmsted, M. Asta, A. Dick, D. Shin, Y. Wang, L. Q. Chen and Z. K. Liu, *CALPHAD: Comput. Coupling Phase Diagrams Thermochem.*, 2013, **42**, 13–18.
65 A. A. Emery and C. Wolverton, *Sci. Data*, 2017, **4**, 170153.
66 M. Aykol, S. S. Dwaraknath, W. Sun and K. A. Persson, *Sci. Adv.*, 2018, **4**, eaaq0148.
67 A. Wold, W. Kunnmann, R. J. Arnott and A. Ferretti, *Inorg. Chem.*, 1964, **3**, 545–547.
68 M. A. Espinosa-Medina, G. Carbajal-De la Torre, H. B. Liu, A. Martínez-Villafañe and J. G. González-Rodriguez, *Corros. Sci.*, 2009, **51**, 1420–1427.
69 A. A. Emery, J. E. Saal, S. Kirklin, V. I. Hegde and C. Wolverton, *Chem. Mater.*, 2016, **28**, 5621–5634.
70 J. Vieten, *Perovskite Materials Design for Two-Step Solar-Thermochemical Redox Cycles*, Doctoral dissertation, TU Dresden (accepted), 2019.
71 B. Bulfin, L. Hoffmann, L. de Oliveira, N. Knoblauch, F. Call, M. Roeb, C. Sattler and M. Schmücker, *Phys. Chem. Chem. Phys.*, 2016, **18**, 23147–23154.
72 S. Brendelberger, J. Vieten, M. Roeb and C. Sattler, *Int. J. Hydrogen Energy*, 2019, DOI: 10.1016/j.ijhydene.2018.12.135.
73 M. W. Chase and S. National Institute of and Technology, *NIST-JANAF thermochemical tables*, American Chemical Society, American Institute of Physics for the National Institute of Standards and Technology, Washington, D.C., Woodbury, N.Y., 1998.
74 M. de Jong, W. Chen, T. Angsten, A. Jain, R. Notestine, A. Gamst, M. Sluiter, C. Krishna Ande, S. van der Zwaag, J. J. Plata, C. Toher, S. Curtarolo, G. Ceder, K. A. Persson and M. Asta, *Sci. Data*, 2015, **2**, 150009.
75 A. Steinfeld, S. Sanders and R. Palumbo, *Sol. Energy*, 1999, **65**, 43–53.
76 C. Agrafiotis, M. Roeb and C. Sattler, *Renewable Sustainable Energy Rev.*, 2015, **42**, 254–285.
77 S. Brendelberger and C. Sattler, *Sol. Energy*, 2015, **113**, 158–170.
78 J. R. Scheffe, M. Welte and A. Steinfeld, *Ind. Eng. Chem. Res.*, 2014, **53**, 2175–2182.
79 R. Bader, R. Bala Chandran, L. J. Venstrom, S. J. Sedler, P. T. Krenzke, R. M. De Smith, A. Banerjee, T. R. Chase, J. H. Davidson and W. Lipiński, *J. Sol. Energy Eng.*, 2015, **137**, 031007.
80 S. Brendelberger, H. von Storch, B. Bulfin and C. Sattler, *Sol. Energy*, 2017, **141**, 91–102.
81 J. Felinks, M. Lange and F. Call, DE102013209658A1, 2014.
82 J. R. Jennings, *Catalytic Ammonia Synthesis: Fundamentals and Practice*, Springer US, 2013.

83 R. Lan, J. T. S. Irvine and S. Tao, *Sci. Rep.*, 2013, **3**, 1145.
84 E. Marek, W. Hu, M. Gaultois, C. P. Grey and S. A. Scott, *Appl. Energy*, 2018, **223**, 369–382.
85 S. Brendelberger, J. Vieten, M. J. Vidyasagar, M. Roeb and C. Sattler, *Sol. Energy*, 2018, **170**, 273–279.
86 M. Ezbiri, K. M. Allen, M. E. Gàlvez, R. Michalsky and A. Steinfeld, *ChemSusChem*, 2015, **8**, 1966–1971.
87 P. R. N. Silva and A. B. Soares, *Ecletica Quim.*, 2009, **34**, 31–38.
88 C. L. Muhich, S. Blaser, M. C. Hoes and A. Steinfeld, *Int. J. Hydrogen Energy*, 2018, **43**, 18814–18831.
89 S. Li, V. M. Wheeler, P. B. Kreider and W. Lipiński, *Energy Fuels*, 2018, **32**, 10838–10847.
90 B. Bulfin, *Phys. Chem. Chem. Phys.*, 2019, **21**, 2186–2195.

